Molecular-scale simulation of electroluminescence in a multilayer white OLED

Murat Mesta[1], Marco Carvelli[1,2,3], Rein J. de Vries[1,2,3], Harm van Eersel[1,2], Jeroen J.M. van der Holst[1], Matthias Schober[4], Mauro Furno[4], Björn Lüssem[4], Karl Leo[4], Peter Loebl[5], Reinder Coehoorn[1,2] & Peter A. Bobbert[1*]

[1]*Department of Applied Physics, Technische Universiteit Eindhoven, P.O. Box 513, NL-5600 MB Eindhoven, The Netherlands*

[2]*Philips Research Laboratories, High Tech Campus 4, NL-5656 AE Eindhoven, The Netherlands*

[3]*Dutch Polymer Institute, P.O. Box 902, NL-5600 AX Eindhoven, The Netherlands*

[4]*Institut für Angewandte Photophysik, Technische Universität Dresden, George-Bähr-Strasse 1, D-01062 Dresden, Germany*

[5]*Philips Research Aachen, Weisshausstrasse 2, D-52066 Aachen, Germany*

**e-mail: p.a.bobbert@tue.nl*

In multilayer white OLEDs the electronic processes in the various layers -injection and motion of charges as well as generation, diffusion, and radiative decay of excitons- should be concerted such that efficient, stable, and colour-balanced electroluminescence can occur. Here we show that it is feasible to carry out Monte Carlo simulations including all these molecular-scale processes for a hybrid multilayer OLED combining red and green phosphorescent layers with a blue fluorescent layer. The simulated current density and emission profile are shown to agree well with experiment. The experimental emission profile was obtained with

nanometre resolution from the measured angle- and polarization-dependent emission spectra. The simulations elucidate the crucial role of exciton transfer from green to red and the efficiency loss due to excitons generated in the interlayer between the green and blue layer. The perpendicular and lateral confinement of the exciton generation to regions of molecular-scale dimensions revealed by this study demonstrate the necessity of molecular-scale instead of conventional continuum simulation.

Organic light-emitting diodes (OLEDs) hold great promise for energy-efficient light sources with unique properties. In contrast to inorganic LEDs they have a large light-emitting area and can be fabricated on flexible substrates. The development of white OLEDs for lighting applications is particularly challenging, since these require the combination of emitters of different colours. They should function such that 1) electrical energy is efficiently converted into light, 2) the right colour balance is obtained, and 3) long-term stability of the efficiency and colour balance is guaranteed. A well-established strategy to achieve these goals is the use of multilayer stacks, where each layer performs a specific function[1]. Control of all the electronic processes occurring in such stacks – injection and transport of charges as well as generation, diffusion, and radiative decay of excitons– is necessary, but at the same time extremely complex. The development of predictive modelling of these processes is imperative, but has not yet been realized.

The efficiency of white OLEDs has been increased by introducing highly n- and p-doped organic-semiconductor layers at the injecting contacts in combination with layers transporting electrons and holes to the emission layers[2], and phosphorescent triplet emitters harvesting al-

most all singlet and triplet excitons formed in the emission layers[3]. Full-phosphorescent OLEDs use red, green, and blue triplet emitters, and are among the most efficient[4]. An issue with these OLEDs, however, is the long-term instability of the available blue triplet emitters. Therefore, most present commercial white OLEDs are hybrid, generating the blue component of the emitted light by fluorescence[5,6]. Nevertheless, long-term stability of OLEDs remains a concern and it is of utmost importance to identify causes for their degradation.

Charge transport in the organic semiconductors used in OLEDs occurs by hopping between sites with an energy disorder that is often taken to be Gaussian[7]. Advanced OLED simulation methods have been developed based on this concept that treat the device as a continuous one-dimensional (1D) system, with properties depending only on the distance to the electrodes[8–11]. For a single-layer OLED with a thick organic layer such a method was applied with considerable success[11]. In white OLED stacks, molecular-scale inhomogeneities in the stacking direction caused by sublayer thicknesses of only a few molecular diameters prevent the use of these methods. 1D approaches with discretisation in the stacking direction[12,13] would then be more appropriate. However, these cannot capture the lateral molecular-scale inhomogeneities in the exciton generation revealed by the present study.

Here, we carry simulation of OLED electroluminescence to a next level by presenting the first three-dimensional (3D) molecular-scale Monte Carlo simulations of all relevant electronic processes in a white OLED. Apart from charge injection, charge transport, and exciton formation, the simulations contain for the first time effects of 3D exciton diffusion. As demonstration and

validation we apply the simulations to a white hybrid OLED stack that we have fabricated. We compare the simulation results for the current-voltage characteristics and the emission profile to experiments on this stack. The results provide a unique view on where and how luminescence occurs, on molecular-scale inhomogeneities in the exciton generation, on efficiency-loss processes, and on possible causes for degradation. The range of applicability of the developed simulation tools is broad and we foresee their use in future optimized OLED stack design.

Electrical and optical characteristics

Figure 1a shows the schematic layer structure of the investigated OLED stack and the materials used in the different layers (see Methods section for its fabrication). Its working principle is as follows. Holes reach the inner part of the stack by injection from an ITO layer into a p-doped injection layer and transport through a hole-transporting and electron-blocking layer of α-NPD, and electrons do so by injection from an aluminium cathode into an n-doped electron-injection layer and transport through an electron-transporting and hole-blocking layer of NET5. In the inner part of the stack, blue light is generated in a fluorescent Spiro-DPVBi layer adjacent to the NET5 layer. Green light is generated in a TCTA layer doped with the green phosphorescent dye Ir(ppy)$_3$ and red light in an α-NPD layer doped with the red phosphorescent dye Ir(MDQ)$_2$(acac).

The green phosphorescent layer is separated from the blue fluorescent layer by an interlayer consisting of a mixture of an electron and a hole transporter, TPBi and TCTA. The purpose of this interlayer is twofold[5]. Firstly, it blocks the transfer of singlet excitons from the blue to the green

layer and of triplet excitons from the green to the blue layer (Spiro-DPVBi has a triplet energy lower than that of Ir(ppy)$_3$). Secondly, the interlayer allows passage of electrons from the blue to the green layer and of holes from the green to the blue layer. There is no equivalent interlayer between the green and red phosphorescent layers. Therefore, triplet excitons can diffuse from the green to the red layer and this is in fact an important process in establishing the right colour balance.

The measured room-temperature current density-voltage characteristic of the OLED is shown in Fig. 1b. At a bias around 2.5 V the OLED switches on and the current is measured up to 4.2 V. At higher voltages, there is a risk of permanently damaging the OLED by excessive heating. Unless stated otherwise, for all other presented results the bias is 3.6 V. The CIE 1931 colour point of the perpendicularly emitted light at this bias was measured to be $[x, y] = [0.47, 0.45]$. It corresponds to warm-white emission, slightly shifted to the yellow/orange. The external quantum efficiency (EQE) –the fraction of emitted photons per injected electron-hole pair– is $5 \pm 1\%$, as measured in an integrating sphere setup.

The colour-resolved emission profile of the OLED is shown in Fig. 2a. The profile was reconstructed from the measured angle and polarization dependent emission spectra, as pioneered in ref. 14 for a single-layer OLED and here applied for the first time to an OLED stack (see Methods section). The nanometre-scale resolution of the reconstruction method fully pays off in the present context, since the emission occurs in each layer in a region of only a few nanometres thick. In the blue layer, the emission occurs close to the interface with the interlayer. Detailed

resolution of the emission profile within the very thin green layer (3 nm) is beyond the accuracy of the reconstruction method. The emission from the red layer occurs close to the interface with the green layer and can be due to excitons generated in this layer as well as to exciton transfer from the green to the red layer. The emission percentages in the different emission layers are indicated in the figure. Almost no dependence of the colour point and reconstructed emission profile on the bias was found in a range of about 1 V around 3.6 V. Using the outcoupling properties of the stack, the expected colour point was calculated from the reconstructed emission profile. The result, again $[0.47, 0.45]$, perfectly agrees with the directly measured colour point, demonstrating the internal consistency of the reconstruction procedure.

By using the radiative decay probabilities η_{r} of the different emitters, the reconstructed emission profile also allows a calculation of the expected EQE. We take $\eta_{\mathrm{r}} = 0.35$ for the blue fluorescent emitter[15], and 0.84 and 0.76 for the red and green phosphorescent emitter in their respective hosts[16]. The exciton generation efficiency can be assumed to be unity because of the effective confinement of electrons and holes to the inner part of the stack by the charge-blocking layers. By assuming that in the blue fluorescent layer singlet and triplet excitons are generated in a quantum-statistical ratio of 1:3, and using the calculated light-outcoupling efficiency, we find an EQE of $9 \pm 1\%$. This is substantially larger than the measured EQE of $5 \pm 1\%$, which indicates that, apart from the limited outcoupling efficiency ($20 \pm 1\%$), the quantum-statistically limited number of singlet excitons formed in the blue layer, and the limited radiative decay probabilities of the emitters, there are other factors that limit the efficiency of this OLED. Simulation of the electronic processes occurring in the OLED provides a unique tool to investigate this.

Monte Carlo simulation of charge and exciton dynamics

The feasibility of performing Monte Carlo simulations at the molecular level of charge injection and transport in single-layer single-carrier devices of disordered organic semiconductors has recently been demonstrated[17]. Here, we carry such simulations to a next level by applying them to the OLED stack of Fig. 1a and including exciton generation and diffusion (see Methods section). The molecules in the stack are represented by point sites arranged on a cubic lattice with a lattice constant $a = 1$ nm, the typical intermolecular distance of the materials comprising the stack. We assume the presence of correlated disorder in the electron and hole energies, which was found to be present in various small-molecule materials[18,19]. The disorder is assumed to be caused by random dipoles and has a strength $\sigma = 0.1$ eV, corresponding to the value found for hole transport in α-NPD[18]. We expect that with this the hole transport in α-NPD is properly described and that also a reasonable description is obtained for the charge transport in the other materials in the stack. Red and green emitting guests are introduced according to the known concentration of the emitters, with appropriately adapted energy levels.

Electron traps are ubiquitous in organic semiconductors and are introduced in the layers in which electron transport is important: the blue fluorescent layer and the electron-transporting layer. Their presence is modelled using an exponential distribution of trap energies[20–22] with a concentration c_{trap} and a trap energy $k_{\mathrm{B}}T_0$. Transport in electron-only devices of the electron transporter BAlq could be modelled well using correlated disorder with $\sigma = 0.09$ eV, $c_{\mathrm{trap}} = 7 \times 10^{-4}$, and a trap temperature $T_0 = 1200$ K[19], demonstrating the applicability of our method of

introducing traps in molecular semiconductors.

We take Miller-Abrahams rates for the nearest-neighbour hopping of charges on the lattice[23]. Modelling of charge transport in devices of small-molecule semiconductors based on these rates has been very successful[18,19]. It was recently demonstrated that the charge-transport properties found with these rates are very similar to those with the often used Marcus hopping rates[24] (the latter rates would require the introduction of another parameter, the reorganization energy[25]). The energy differences in the hopping rates contain, apart from the random site energies, an electrostatic contribution due to the bias applied to the OLED and the Coulomb energy due to all present charges. We treat the doped injection layers as metallic, injecting and collecting charges with an energy according to a given work function. Exciton generation occurs by hopping of an electron to a site where a hole resides, or vice versa.

In Table 1 we give the parameters of the stack materials as used in the simulations of the charge dynamics. Figure 3 pictures the level scheme of the centres of the HOMO (highest occupied molecular orbital) and LUMO (lowest unoccupied molecular orbital) energy distributions for holes and electrons. The parameters were determined from charge-transport and spectroscopic studies of the various materials. The Supplementary Information contains a detailed explanation of how the parameters in Table 1 were obtained and a sensitivity analysis of the simulation results to variations in these parameters.

Exciton diffusion within and in between the green and red layers is included in the simulations (see Methods section). Because the red and green triplet emitters trap electrons as well as

holes (see Fig. 3), most excitons in the red and green layer are generated on the emitters. We describe the diffusion of excitons among the emitters by Förster transfer, made possible by mixing in of spin-singlet character into the exciton wave function due to the spin-orbit coupling of the heavy iridium atoms. The Förster transfer rate between two emitters i and j is[26]

$$k_{ij} = \frac{1}{\tau_{\mathrm{r},i}} \left(\frac{R_{0,ij}}{R} \right)^6 , \tag{1}$$

with $\tau_{\mathrm{r},i}$ the radiative lifetime of emitter i, R the distance between the two emitters, and $R_{0,ij}$ the Förster radius for transfer from i to j. The latter accounts for the spectral overlap between the emission spectrum of i and the absorption spectrum of j. Apart from undergoing transfer, the excitons can decay radiatively with a rate $k_{\mathrm{r},i} = 1/\tau_{\mathrm{r},i}$, or non-radiatively with a rate $k_{\mathrm{nr},i} = 1/\tau_{\mathrm{nr},i}$. These rates are related to the radiative decay probabilities by $\eta_{\mathrm{r},i} = k_{\mathrm{r},i}/(k_{\mathrm{r},i} + k_{\mathrm{nr},i})$. The parameters used in the exciton dynamics, taken from literature, are given in Table 2. The large Förster radius $R_{0,\mathrm{GR}} = 3.5$ nm taken for transfer from green to red[27] reflects the large spectral overlap for this transfer. Transfer from red to green is neglected since it will only occur with a very small rate. Simulation of exciton diffusion is performed for each exciton generated in the red or green layer and proceeds independently from all other processes, which means that exciton-exciton and exciton-charge interactions are neglected. The excitons generated on host sites in the red and green layer (a minority) are assumed to transfer instantaneously to triplet emitter guests in their neighbourhood. Diffusion of excitons generated in the blue layer is not taken into account, because their diffusion length will be short and because transfer to the green layer is blocked by the interlayer. Excitons generated in the interlayer are assumed to be lost by non-radiative decay or emission outside the visible spectrum.

Current density, exciton generation, and light emission

The simulation results for the current density in the OLED at several voltages, using the parameters of Table 1, are given by the symbols in Fig. 1b. The simulated current density curve is close to the measured one. We stress that the parameters of Table 1 come from separate studies of the materials or material combinations in the stack, so that the simulated current density can really be considered as a prediction. The overall agreement between the simulated and measured current density indicates that the charge transport through the stack is well described by the simulations. The larger experimental current density at high voltage could result from a heating effect. The discrepancy at low voltage could be due to a slight underestimation of the trapping of holes by Ir(MDQ)$_2$(acac) in the α-NPD:Ir(MDQ)$_2$(acac) layer. Figures S1b and c in the Supplementary Information show that with a typical experimental uncertainty of about 0.1 eV in the HOMO energies of α-NPD and Ir(MDQ)$_2$(acac) the calculated current density has an uncertainty of about one order of magnitude. We note that the effects of trapping are strongest at small voltages, when the traps are only partially filled, giving rise to an enhanced steepness of the $J(V)$ curve.

In Fig. 2b we display the simulated exciton-generation and light-emission profiles. The emission profile is obtained from the exciton-generation profile and the simulation of exciton diffusion. As in the construction of the experimental emission profile, in the blue layer a 1:3 singlet-triplet exciton-generation ratio was assumed, the radiative decay probability in this layer was taken into account, and no emission from the interlayer was assumed. The resulting emission fractions of the three colours agree well with those of the reconstructed profile in Fig. 2a. The simulated profile

is more broadened than the reconstructed profile, but this is probably due to the limited accuracy of the reconstruction procedure, which tends to produce δ-function shaped profiles when the profile width approaches the resolution limit. From the difference between the simulated exciton-generation and light-emission profiles in the green and red layers the crucial role of interlayer exciton transfer becomes clear. Only a small amount of excitons is generated in the red layer, but due to exciton transfer the emission in the red layer is greatly enhanced to a value that is in agreement with experiment.

A sizable amount, 21%, of the excitons in the simulations is generated in the interlayer in between the green phosphorescent and blue fluorescent layer. Accounting for these excitons, which are assumed not to contribute to the luminescence, the calculated EQE drops from the aforementioned 9 ± 1 to $7\pm1\%$. When comparing this to the measured EQE of $5\pm1\%$ we can say that at least a large part of the difference can be explained by excitons generated in the interlayer. Because of the uncertainty in the measured and calculated EQE, it is hard judge about other possible factors causing the difference. However, we expect that the following factors can play an additional role: 1) exciton quenching due to exciton-exciton and exciton-charge interactions, 2) insufficient blocking by the interlayer of transfer of triplet excitons from the green layer to energetically lower-lying triplet-exciton states in the blue fluorescent layer, and 3) a singlet-triplet generation ratio in the blue fluorescent layer that is smaller than the assumed 1:3 ratio. The narrowness of the profiles in Fig. 2 suggests that exciton quenching could play a role, because of high exciton and charge densities in the exciton-generation and light-emission regions. Simulations in which the dynamics of an exciton is no longer decoupled from that of other excitons and charges should shed light on

this.

Inhomogeneities in exciton generation

The simulations provide access to statistical information about electronic processes that cannot be obtained from a continuum treatment. An analysis of the inhomogeneity in the exciton generation can help in assessing the validity of a continuum treatment for describing this process. Also, it can help in assessing material degradation, since a strongly inhomogeneous distribution will likely lead to local material degradation. The inhomogeneity in the exciton generation in the three emission layers and the interlayer is quantified in Fig. 4, where the fraction of exciton-generation events is plotted as a function of the fraction of sites participating in these events. The strong deviations from a homogeneous distribution (dashed line) points at an extreme inhomogeneity. Figure 4a shows the distribution for the host sites and Fig. 4b that for the phosphorescent guest sites and the traps in the blue layer. The reason for the occurrence of the inhomogeneity is the fact that exciton generation occurs predominantly at sites that either trap electrons or holes[28]. Because in the green and red layer the triplet emitters act as strong traps for both electrons and holes (see Fig. 3), most exciton-generation events take place on the emitters, as corroborated by comparing the numbers of these events indicated in Fig. 4. In these layers, the fraction of host sites on which exciton generation occurs is very low, leading to the observed strong inhomogeneity for these sites. For the electron traps in the blue layer the inhomogeneity is least pronounced. This is because the fraction of these traps is so low that a sizable fraction of them traps an electron and participates in exciton generation. Most exciton-generation events in the blue layer occur on the host sites,

however, and as a result the inhomogeneity in the blue host is not as strong as in the red and green host.

The spatial inhomogeneity in the exciton generation is visualized in Fig. 5. This figure displays the position-dependent exciton generation in six different slices of sites. In line with Fig. 4 it is observed that most exciton-generation events occur on a small fraction of the sites. The inhomogeneity is strongest in the green and red layer, because of the guests in these layers. In the blue layer, the trap fraction is so low that it hardly influences the spatial distribution of the exciton generation (one active trap is visible in Fig. 5f). In addition, strong clustering of exciton generation is observed in all layers, which is due to the correlation in the disorder. This clustering occurs within each slice, but also between adjacent slices in different layers, as becomes clear from comparing Figs. 5a with b, c with d, and e with f.

In conclusion, we have shown in this work that it is possible to perform realistic three-dimensional Monte Carlo simulations at the molecular level of electronic processes leading to electroluminescence in multilayer OLED stacks relevant for lighting applications. The focus was on a particular OLED stack, but the developed simulation tools have a broad range of applicability. We stress that the molecular-scale treatment of the electronic processes in this work was essential, for the following reasons: 1) some of the layers in the stack have a thickness of only a few nanometres, i.e., a few molecular diameters, leading to strong perpendicular gradients in the electric field and the concentrations of charge-carriers and excitons, 2) the exciton-generation and light-emission profiles have a width of only a few nanometres, even in the layers that are much thicker than a few

nanometres, 3) the distribution of exciton-generation events shows large inhomogeneities at the molecular scale, in the perpendicular and lateral directions, and 4) the presence of phosphorescent guests and traps further enhances the effects of these inhomogeneities. Conventional continuum approaches to simulate electronic processes cannot capture these aspects.

The present work can be considered as the opening of the road towards rational design of multilayer OLED stacks based on molecular-scale modelling of electronic processes. Extensions of the work in various directions are possible. Inclusion of exciton-exciton and exciton-charge quenching processes will be important to assess efficiency loss and material degradation by these processes. Another important extension is the incorporation of information about the microscopic morphology of the stack materials, including the molecular packing and possible dye aggregation, obtained with molecular dynamics or Monte Carlo modelling, and about hopping rates obtained from quantum-chemical calculations[29,30]. This may eventually lead to fully predictive modelling of electroluminescence in OLED stacks. Including these extensions is expected to be feasible without a need for computational resources far exceeding that used in the present work.

Methods

OLED fabrication and layer-thickness control. The OLED was fabricated by thermal evaporation of the organic materials onto ITO-coated, structured glass substrates in an UHV chamber (Kurt J. Lesker Company) with a base pressure around $10-8$ mbar. The thickness of the organic film is monitored during evaporation by quartz crystal microbalances. This allows for a precise control of the organic layer thickness with nanometre precision, which is in particular important for the

deposition of the green emission layer and the interlayer (both 3 nm thick). Furthermore, due to the design of our deposition tool, we observe a very good homogeneity of our films on large areas (less than 5% variation in layer thickness on a 100×100 mm^2 plate), making us confident that the thickness variation of each layer on the length scale of the OLED is very small. Immediately after preparation the OLED was encapsulated under nitrogen atmosphere using epoxy glue and glass lids.

Reconstruction of the emission profile. The technique to reconstruct the emission profile in the OLED is similar to that introduced in ref. 14. It is based on the solution of an inverse outcoupling problem and makes use of the calculated angle, polarization, and wavelength dependence of the emission of the radiation of a dipole in the layer stack, averaged over a uniform distribution of orientations. The complex refractive index dispersion curves and photoluminescence spectra (describing the 'source spectra' for the red, green, and blue emission) entering the calculation of the outcoupling were measured or were obtained from the material library of SETFOS (a commercial software program distributed by Fluxim AG, Switzerland). The discretisation step in the reconstruction procedure was 1 nm. It was assumed that the dipoles of each 'colour' are located in the corresponding emission layer and that no emission takes place at organic-organic interfaces and within the TCTA:TPBi interlayer (the charge-transfer excitons that might be present in these regions are expected to decay non-radiatively or by emitting photons outside the visible spectrum). Since the thickness of the green layer is close to the resolution limit of the reconstruction method, the emission from this layer was assumed to come from its centre. The light emission under an angle θ with the sample normal was measured through a glass hemisphere applied to the glass side

of the OLED, with an index-matching fluid in between.

The shape of the emission profile is obtained in the following way using a least-mean-squares fitting method. As a first step, the experimental s- and p-polarized emission intensities $I^{\rm expt}_{s(p)}(\lambda,\theta)$, measured at M values of the wavelength λ and N values of the emission angle θ, are normalized using the expression

$$I^{\rm expt}_{\rm norm,s(p)}(\lambda,\theta) = \frac{I^{\rm expt}_{s(p)}(\lambda,\theta)}{S^{\rm expt}_{s(p)}(\lambda)}\ , \tag{2}$$

with

$$S^{\rm expt}_{s(p)}(\lambda) \equiv \max(I^{\rm expt}_{s(p)}(\lambda,\theta)). \tag{3}$$

The maximum $\max(I^{\rm expt}_{s(p)}(\lambda,\theta))$ is calculated over the entire wavelength and angle range, separately for *s*- and *p*-polarized light.

As a second step, trial intensity functions are calculated. A normalized fixed source spectrum $S^{\rm source}_{\rm k}(\lambda)$, a trial emission profile $P_{{\rm k},\delta}$ depending on layer (k) and position (δ, in 1 nm steps), and a trial dipole orientation θ_d are assumed. The emission profile is normalized such that:

$$\sum_{k=1}^{k_{\rm max}} \sum_{\delta} P_{k,\delta} = 1. \tag{4}$$

The trial calculated intensity is then:

$$I^{\rm calc,trial}_{s(p)}(\lambda,\theta) = \sum_{k=1}^{k_{\rm max}} \sum_{\delta} P_{k,\delta} S^{\rm source}_{k}(\lambda) I^{\rm calc}_{s(p)}(\lambda,\theta,k,\delta,\theta_d). \tag{5}$$

The intensity due to emission from a single dipole at position δ in layer k, $I^{\rm calc}_{s(p)}(\lambda,\theta,k,\delta,\theta_d)$, includes the radiative decay probability in layer k, corrected for microcavity effects. Subsequently,

the trial intensity is normalized:

$$I^{\mathrm{calc,trial}}_{\mathrm{norm,s(p)}}(\lambda,\theta) = \frac{I^{\mathrm{calc,trial}}_{s(p)}(\lambda,\theta)}{\max(I^{\mathrm{calc,trial}}_{s(p)}(\lambda,\theta))}, \tag{6}$$

where the maximum $\max(I^{\mathrm{calc,trial}}_{s(p)}(\lambda,\theta))$ is calculated in the same way as $\max(I^{\mathrm{expt}}_{s(p)}(\lambda,\theta))$. As a final step, the optimal emission profile and dipole orientation are determined by iteratively minimizing the quantity

$$\chi^2 \equiv \sum_{i=1}^{M}\sum_{j=1}^{N}\sum_{s,p}\left\{I^{\mathrm{calc,trial}}_{\mathrm{norm,s(p)}}(\lambda_i,\theta_j) - I^{\mathrm{expt}}_{\mathrm{norm,s(p)}}(\lambda_i,\theta_j)\right\}^2 . \tag{7}$$

Simulation procedure. The Monte Carlo simulations were performed on a cubic lattice of 50×50×56 sites representing the molecules in the OLED stack, with periodic boundary conditions in the lateral (x- and y-) directions. An energy landscape with correlated disorder was generated by taking a cubic lattice of sites, with a size in the z-direction larger than the thickness of the stack, placing on each site a randomly oriented static dipole, and calculating the resulting electrostatic field at each site (excluding the dipole at that site). Normalization is such that the nearly Gaussian density of states has a standard deviation $\sigma = 0.1$ eV [The resulting energetic disorder is not perfectly Gaussian, because the precise conditions for the validity of the central-limit theorem are not met. However, this leads to only subtle differences[32]]. The red and green emitting guests were introduced in the simulations by offsets, with respect to the surrounding host material, of the HOMO and LUMO energies of sites that were randomly selected according to the concentration of the emitters. Electron traps were introduced by random site selection according to the concentration c_{trap} in the blue fluorescent layer (Spiro-DPVBi) and the electron-transporting layer (NET5). The LUMO energies of the assigned electron traps were drawn from an exponential distribution,

$(k_{\mathrm{B}}T_0)^{-1}\exp([E - E_{\mathrm{LUMO,host}}]/k_{\mathrm{B}}T_0)$ if $E < E_{\mathrm{LUMO,host}}$ and otherwise 0, where $E_{\mathrm{LUMO,host}}$ is the centre energy of the Gaussian distribution of the LUMO energies of the surrounding host sites. The HOMO energies of the trap sites were not changed.

Miller-Abrahams rates[23] were taken for the hopping of charges on the lattice. These are given by $\nu_0 \exp(-2\alpha R + \Delta E/k_{\mathrm{B}}T)$ for energetically upward hops (energy difference $\Delta E > 0$) and $\nu_0 \exp(-2\alpha R)$ for energetically downward hops ($\Delta E < 0$), where $k_{\mathrm{B}}T$ is the thermal energy, α an inverse wave function decay length, and R the distance over which the hop takes place. In the case of nearest-neighbour hopping considered by us, the prefactor ν_0 (representing a typical phonon frequency) together with the factor $\exp(-2\alpha a)$ yield a prefactor that was adjusted to reproduce the room-temperature charge-carrier mobility μ_0 at vanishing electric field and charge-carrier concentration of the material under consideration. The energy difference ΔE for a hop of a charge from one site to another contains, apart from the random site energies discussed above, an electrostatic contribution due to the applied bias over the OLED and the Coulomb interaction with all other charges. The latter contribution was calculated as in ref. 17 by a separation into a short-range part due to charges within a sphere of radius R_{c} and a long-range part due to charges outside this sphere, for which a layer-average was taken. A cut-off radius of $R_{\mathrm{c}} = 8$ sufficed in our case. The relative dielectric constants of the layers in the stack are all quite similar and we took them all equal to $\epsilon_{\mathrm{r}} = 3.5$, simplifying the calculation of electrostatic energies. We treated the doped injection layers as metals with a given work function. Injection of holes and electrons from these layers into the adjacent hole and electron transporting layers was treated in the same way as in ref. 17, with inclusion of an image-charge potential. Exciton generation occurs by hopping of an

electron to a site where a hole resides, or vice versa, and is assumed to be always an energetically downward process.

From the room-temperature mobilities μ_0 of holes (h) and electrons (e) of the host materials at low field and low carrier density the hopping frequencies ν_0 were determined using the parameterization in ref. 9 of the mobility. The precise values of $\nu_{0,\mathrm{h,e}}$ for hops in between host sites and guest or trap sites are found not to be important[31] and for simplicity we took them equal to the values in the host. For ν_0 involving hops between sites across an organic-organic interface we took the geometric mean of the bulk values at either side of the interface.

All simulations started with an empty device and an applied bias. A steady-state situation was obtained after typically 2×10^9 Monte Carlo steps, which was judged from the uniformity of the charge current in the z-direction. Subsequently, the current density and the exciton-generation profile were determined from typically another 2×10^9 Monte Carlo steps. For voltages below 2.6 V it was not possible to obtain a statistically significant value for the current density. By repeating the simulations for different disorder configurations we conclude that the error in the reported current density in Fig. 1b is about 10% and that the error in the reported fractions of exciton generation and light emission in the various layers in Fig. 2 is about 1% or smaller.

Exciton diffusion was simulated for excitons generated in the green and red layer and started from the calculated exciton generation distribution. An exciton on a triplet emitter was either removed with a probability according to its total (radiative and non-radiative) decay rate or transferred to another emitter. In the latter case an exciton-accepting emitter was selected according to

Eq. (1). The process continued until each exciton was removed, after which the number of excitons decaying radiatively in each layer was counted. An exciton initially generated on a host site was instantaneously transferred to a guest emitter site selected according to Eq. (1).

References

1. Kido, J., Kimura, M. & Nagai, K. Multilayer white light-emitting organic electroluminescent device. *Science* **267**, 1332–1334 (1995).

2. Walzer, K., Maennig, B., Pfeiffer, M. & Leo, K. Highly efficient organic devices based on electrically doped transport layers. *Chem. Rev.* **107**, 1233–1271 (2007).

3. Baldo, M. A. *et al.* Highly efficient phosphorescent emission from organic electroluminescent devices. *Nature* **395**, 151–154 (1998).

4. Reineke, S. *et al.* White organic light-emitting diodes with fluorescent tube efficiency. *Nature* **459**, 234–239 (2009).

5. Schwartz, G., Fehse, K., Pfeiffer, M., Walzer, K. & Leo, K. Highly efficient white organic light emitting diodes comprising an interlayer to separate fluorescent and phosphorescent regions. *Appl. Phys. Lett.* **89**, 083509 (2006).

6. Reineke, S. & Baldo, M. Recent progress in the understanding of exciton dynamics within phosphorescent OLEDs. *Phys. Stat. Sol. A*, 1 – 13 (2012) / DOI 10.1002/pssa.201228292.

7. Bässler, H. & Köhler, A. Charge transport in organic semiconductors. *Top. Curr. Chem.* **312**, 1–66 (2012).

8. Pasveer, W. F. *et al.* Unified description of charge-carrier mobilities in disordered semiconducting polymers. *Phys. Rev. Lett.* **94**, 206601 (2005).

9. Bouhassoune, M., van Mensfoort, S. L. M., Bobbert, P. A. & Coehoorn, R. Carrier-density and field-dependent charge-carrier mobility in organic semiconductors with correlated Gaussian disorder. *Org. Elec.* **10**, 437–445 (2009).

10. Schober, M. *et al.* Quantitative description of charge-carrier transport in a white organic light-emitting diode. *Phys. Rev. B* **84**, 165326 (2011).

11. van Mensfoort, S. L. M. *et al.* Predictive modeling of the current density and radiative recombination in blue polymer-based light-emitting diodes. *J. Appl. Phys.* **109**, 064502 (2011).

12. Houili, H., Tutiš, E., Lütjens, H., Bussac, M. & Zuppiroli, L. MOLED: Simulation of multilayer organic light emitting diodes. *Comput. Phys. Commun.* **156**, 108–122 (2003).

13. Coehoorn, R. & van Mensfoort, S. L. M. Effects of disorder on the current density and recombination profile in organic light-emitting diodes. *Phys. Rev. B* **80**, 085302 (2009).

14. van Mensfoort, S. L. M. *et al.* Measuring the light emission profile in organic light-emitting diodes with nanometre spatial resolution. *Nature Photonics* **4**, 329–335 (2010).

15. Li, G. *et al.* Combinatorial study of exciplex formation at the interface between two wide band gap organic semiconductors. *Appl. Phys. Lett.* **88**, 253505 (2006).

16. Furno, M., Meerheim, R., Hofmann, S., Lüssem, B. & Leo, K. Efficiency and rate of spontaneous emission in organic electroluminescent devices. *Phys. Rev. B* **85**, 115205 (2012).

17. van der Holst, J. J. M., van Oost, F. W. A., Coehoorn, R. & Bobbert, P. A. Monte Carlo study of charge transport in organic sandwich-type single-carrier devices: Effects of Coulomb interactions. *Phys. Rev. B* **83**, 085206 (2011).

18. van Mensfoort, S. L. M., Shabro, V., de Vries, R. J., Janssen, R. A. J. & Coehoorn, R. Hole transport in the organic small-molecule material α-NPD: evidence for the presence of correlated disorder. *J. Appl. Phys.* **107**, 113710 (2010).

19. van Mensfoort, S. *et al.* Electron transport in the organic small-molecule material BAlq the role of correlated disorder and traps. *Org. Elec.* **11**, 1408 – 1413 (2010).

20. Mandoc, M. M., de Boer, B., Paasch, G. & Blom, P. W. M. Trap-limited electron transport in disordered semiconducting polymers. *Phys. Rev. B* **75**, 193202 (2007).

21. May, F., Baumeier, B., Lennartz, C. & Andrienko, D. Can lattice models predict the density of states of amorphous organic semiconductors? *Phys. Rev. Lett.* **109**, 136401 (2011).

22. Olthof, S. *et al.* Ultralow doping in organic semiconductors: Evidence of trap filling. *Phys. Rev. Lett.* **109**, 176601 (2012).

23. Miller, A. & Abrahams, E. Impurity conduction at low concentrations. *Phys. Rev.* **120**, 745–755 (1960).

24. Cottaar, J., Koster, L. J. A., Coehoorn, R. & Bobbert, P. A. Scaling theory for percolative charge transport in disordered molecular semiconductors. *Phys. Rev. Lett.* **107**, 136601 (2011).

25. Marcus, R. A. Electron transfer reactions in chemistry. Theory and experiment. *Rev. Mod. Phys.* **65**, 599–610 (1993).

26. Kawamura, Y., Brooks, J., Brown, J. J., Sasabe, H. & Adachi, C. Intermolecular interaction and a concentration-quenching mechanism of phosphorescent Ir(III) complexes in a solid film. *Phys. Rev. Lett.* **96**, 017404 (2006).

27. Steinbacher, F. S., Krause, R., Hunze, A. & Winnacker, A. Triplet exciton transfer mechanism between phosphorescent organic dye molecules. *Phys. Stat. Sol. A* **209**, 340–346 (2012).

28. van der Holst, J. J. M., van Oost, F. W. A., Coehoorn, R. & Bobbert, P. A. Electron-hole recombination in disordered organic semiconductors: Validity of the Langevin formula. *Phys. Rev. B* **80**, 235202 (2009).

29. Kwiatkowski, J. J. *et al.* Simulating charge transport in tris(8-hydroxyquinoline) aluminium (Alq3). *Phys. Chem. Chem. Phys.* **10**, 1852–1858 (2008).

30. Rühle, V. *et al.* Microscopic simulations of charge transport in disordered organic semiconductors. *J. Chem. Theor. Comp.* **7**, 3335–3345 (2011).

31. Cottaar, J., Coehoorn, R. & Bobbert, P. A. Field-induced detrapping in disordered organic semiconducting host-guest systems. *Phys. Rev. B* **82**, 205203 (2010).

32. Cottaar, J., Coehoorn, R. & Bobbert, P. A. Scaling theory for percolative charge transport in molecular semiconductors: Correlated versus uncorrelated energetic disorder. *Phys. Rev. B* **85**, 245205 (2012).

33. Material supplied by Novaled, AG.

34. Mladenovski, S., Reineke, S. & Neyts, K. Measurement and simulation of exciton decay times in organic light-emitting devices with different layer structures. *Opt. Lett.* **34**, 1375–1377 (2009).

35. Tang, K.-C., Liu, K. L. & Chen, I.-C. Rapid intersystem crossing in highly phosphorescent iridium complexes. *Chem. Phys. Lett.* **386**, 437 – 441 (2004).

36. Schwartz, G., Reineke, S., Rosenow, T., Walzer, K. & Leo, K. Triplet harvesting in hybrid white organic light-emitting diodes. *Adv. Funct. Mater.* **19**, 1319–1333 (2009).

Acknowledgements. This research was supported by the European Community (Program No. FP7-213708 (AEVIOM), M.S., M.F., B.L., K.L., P.L., R.C., and P.A.B.), the Dutch nanotechnology programs NanoNed (J.J.M.v.d.H.) and NanoNextNL (M.M., H.v.E.), and the Dutch Polymer Institute (DPI), projects No. 518 (M.C.) and 680 (R.J.d.V.). The authors thank Dr. Jeroen Cottaar, Dr. Herman Nicolai, Dr. Robert Nitsche, Prof.dr. Beat Ruhstaller, Prof.dr. Paul Blom, and Prof.dr. Neil Greenham for the many discussions we had at the AEVIOM meetings and other occasions. The value of the hole mobility of α-NPD in Table 1 was established with help of Dr. Robert Nitsche. M. de Vries performed the measurements from which the parameter values for NET5 and Spiro-DPVBi in Table 1 were obtained. We acknowledge the contributions of F.W.A. van Oost to the simulation codes.

Author contributions. M.M. and M.C. contributed equally to the work: M.M. performed the main Monte Carlo simulations and M.C. the main measurements on the OLED; R.J.d.V. determined the electron transport parameters in Spiro-DPVBi and NET5; H.v.E. programmed the exciton diffusion software and made part of the figures; J.J.M.v.d.H. was involved in setting up the Monte Carlo simulations; M.S. and M.F. fabricated the OLED, provided its experimental optimization and characterization, and determined hole transport parameters, all supervised by B.L. and K.L.; P.L. was involved in the definition of the OLED stack, the UPS and optical measurements on the stack materials, and the fabrication of devices for the determination of electron transport parameters; R.C. supervised the whole project and contributed to the writing; P.A.B. supervised the simulation work and wrote the main part of the manuscript.

Competing Interests. The authors declare that they have no competing financial interests.

Correspondence. Correspondence and requests for materials should be addressed to P.A.B.

Figure captions

Figure 1: OLED stack and its electrical characteristics. a, Layer structure of the hybrid OLED stack studied in this work (surface area: 2.7 by 2.5 mm). The layers and the used organic materials are, from bottom to top: p-doped hole-injecting layer of NHT5 with 4 mol% NDP2[33], hole-transporting layer of N,N'-di(naphthalen-1-yl)-N,N'-diphenyl-benzidine (α-NPD), layer of α-NPD with 5 mol% of the red phosphorescent dye (acelylacetonate)bis(2-methyldibenzo[f,h]-quinoxinalate)iridium ($Ir(MDQ)_2(acac)$), layer of 4,4',4"-tris(N-carbazoyl)-triphenylamine (TCTA) with 8 mol% of the green phosphorescent dye fac-tris(2-phenylpyridyl)iridium ($Ir(ppy)_3$), interlayer consisting of a mixture of the hole transporter TCTA with 33 mol% of the electron transporter 1,3,5-tris[N-phenylbenzimidazol-2-yl)benzene (TPBi), blue fluorescent layer of 2,2',7,7'-tetrakis(2,2-diphenylvinyl)Spiro-9,9'-bi fluorene (Spiro-DPVBi), electron-transporting layer of NET5[33], and n-doped electron-injecting layer of NET5 with 4 mol% NDN1[33]. **b**, Measured (full) and simulated (symbols, error: $\sim$10%, and dashed curve as guide to the eye) current density-voltage characteristics. The arrow indicates the current density-voltage point at which most reported experimental and simulation studies were performed.

Figure 2: Light-emission and exciton-generation profiles. a, Reconstructed experimental light-emission profile. **b**, Simulated exciton-generation (top) and light-emission (bottom) profile, with the difference caused by excitonic processes. The numbers indicate the fractions in the various layers (errors: $\sim$1% or smaller).

Figure 3: Energy-level diagram. HOMO and LUMO energies in eV of the materials in the

OLED stack of Fig. 1a as used in the simulations, in each case defined as the energy at the top of a Gaussian density of states with standard deviation $\sigma = 0.1$ eV. The horizontal arrows indicate the work functions used for the doped hole and electron injecting layers. The concentrations of the red and green dye are 5×10^{-2} and 8×10^{-2}, respectively. The electron traps in the Spiro-DPVBi and NET5 have concentrations of 10^{-3} and 5×10^{-3}, and trap energies of $k_{\mathrm{B}}T_0 = 0.2$ and 0.12 eV, respectively.

Figure 4: Inhomogeneity in exciton generation. **a**,**b**, Fraction of exciton generation events in the three emission layers and the interlayer as a function of involved fraction of sites. **a**, For the host sites. **b**, For the phosphorescent guest sites in the red and green layers and the electron traps in the blue layer. The total number of generation events is indicated for each type of site. The straight line segments visible in the final parts of the curves are due to the sites at which only a few generation events occur. A homogeneous distribution of generation events would follow the dashed line.

Figure 5: Spatial distribution of exciton generation. **a**-**f**, Distribution of exciton generation in six slices of sites, at positions in the stack indicated by the black lines in the bars at the top of each panel. The dark and bright colours indicate host and phosphorescent guest sites (**a**-**c**) or traps (**f**), respectively. Black and grey (**d**,**e**) indicate TCTA (hole transporter) and TPBi (electron transporter) sites, respectively.

Table captions

Table 1: Material parameters: charge dynamics. HOMO and LUMO energies, room-temperature hole- and electron-mobilities $\mu_{0,\mathrm{h}}$ and $\mu_{0,\mathrm{e}}$ at low field and low carrier density, electron-trap concentration c_{trap}, and trap temperature T_0 of the trap distribution in the different layers of the stack, as used in the Monte Carlo simulations.

Table 2: Material parameters: exciton dynamics. Radiative and non-radiative exciton decay rates k_{r} and k_{nr}, Förster radii R_0 for exciton transfer between triplet emitter molecules, and triplet energies E_{T}. For the green emitting Ir(ppy)$_3$ k_{r} and k_{nr} are taken from ref. 34, while for the red emitting Ir(MDQ)$_2$(acac) k_{r} is obtained from ref. 35 and k_{nr} from η_{r} given in ref. 16 and the relation $\eta_{\mathrm{r}} = k_{\mathrm{r}}/(k_{\mathrm{r}} + k_{\mathrm{nr}})$. A typical value is taken for the value of R_0 for transfer between the same emitter molecules from ref. 26. For the transfer from a green to a red emitter we take $R_{0,\mathrm{GR}} = 3.5$, according to the estimate in ref. 27. The triplet energies are taken from ref. 36.

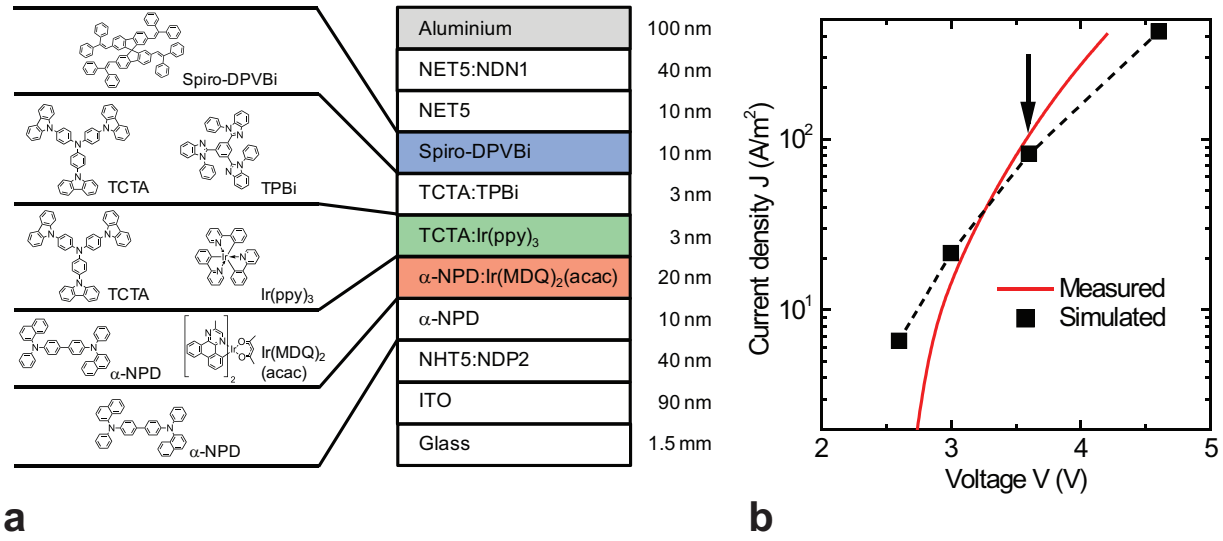

Figure 1: OLED stack and its electrical characteristics.

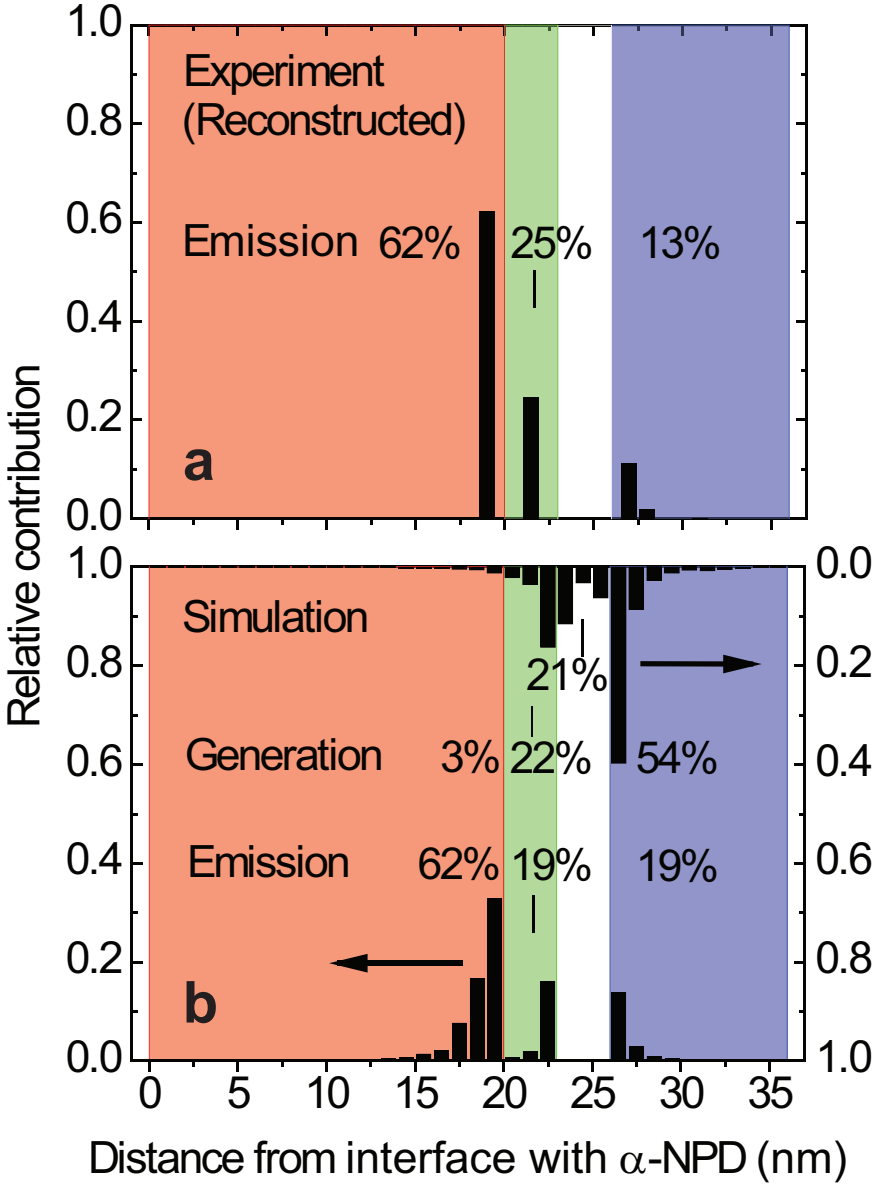

Figure 2: Light-emission and exciton-generation profiles.

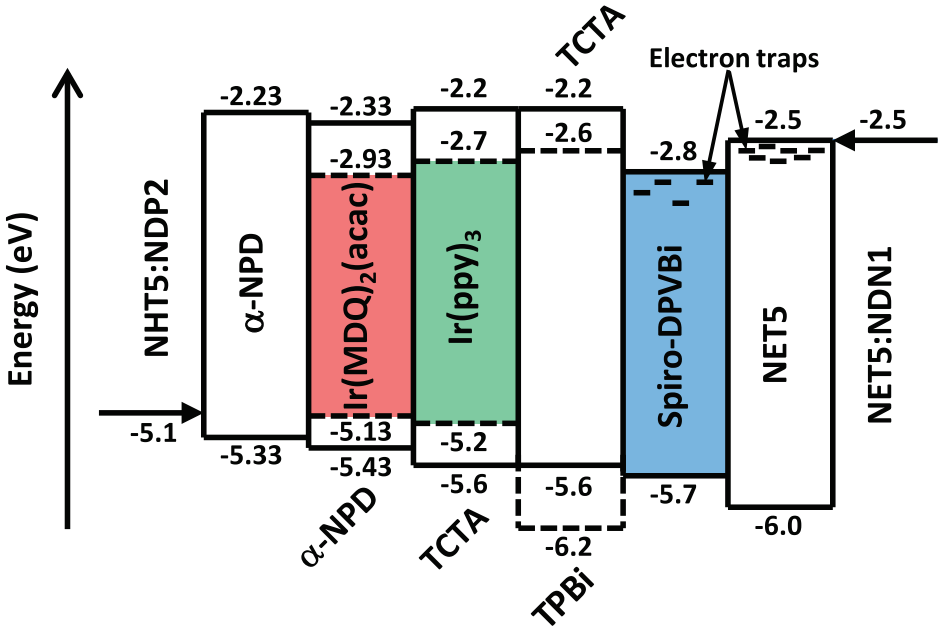

Figure 3: Energy-level diagram.

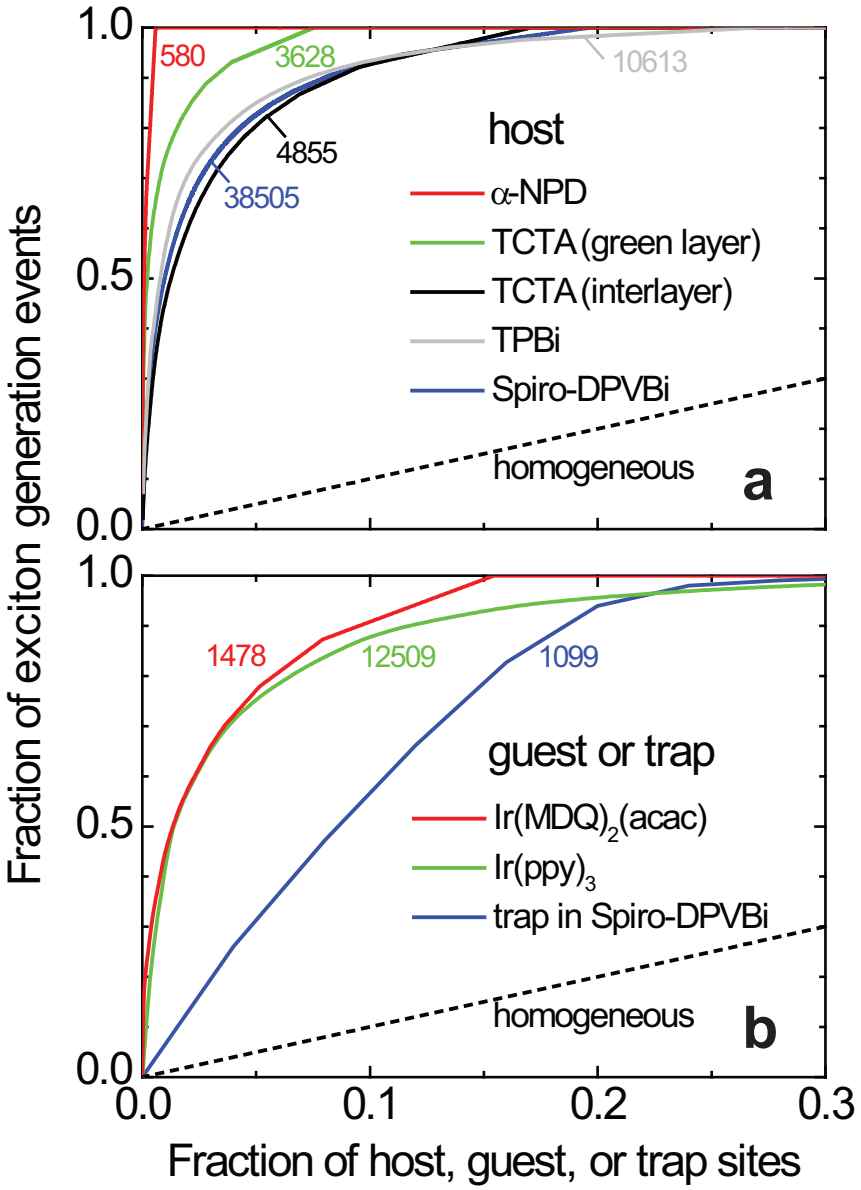

Figure 4: Inhomogeneity in exciton generation.

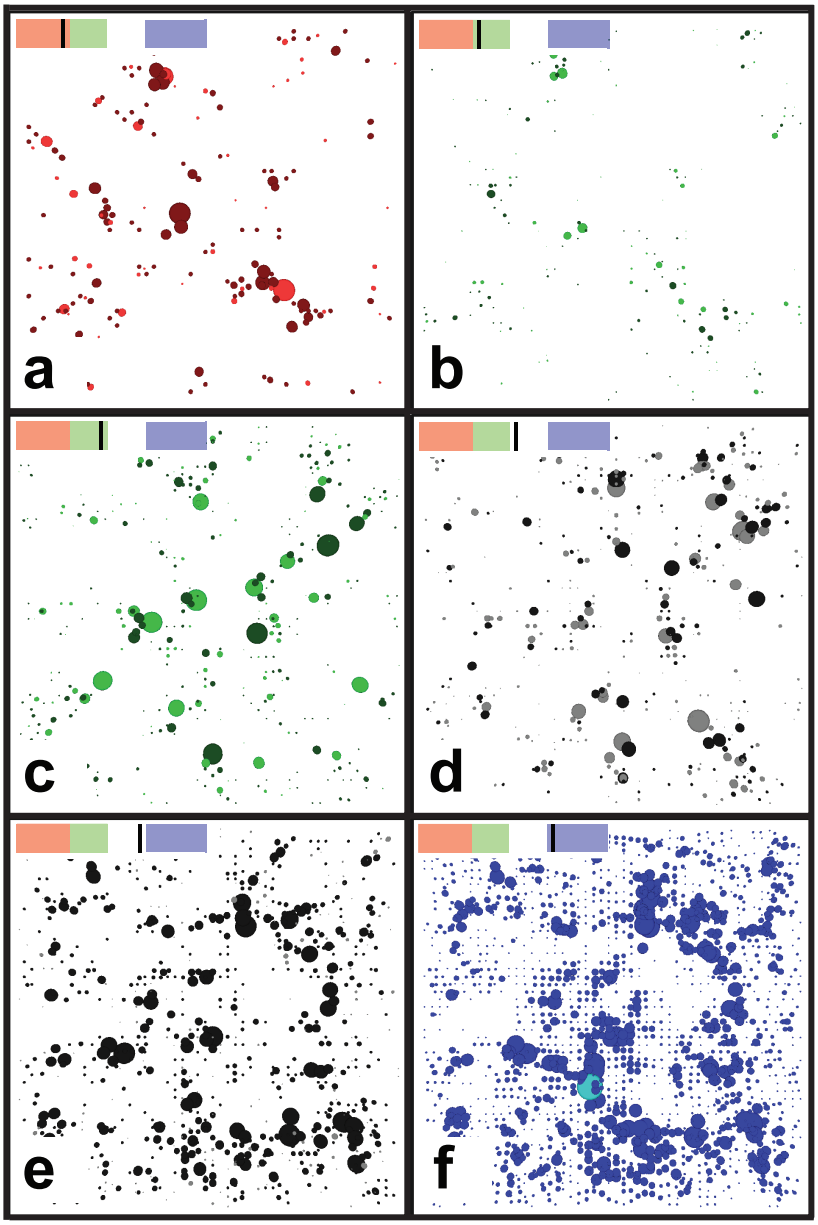

Figure 5: Spatial distribution of exciton generation.

Material	E_{HOMO} (eV)	E_{LUMO} (eV)	$\mu_{0,\mathrm{h}}$ (m^2/Vs)	$\mu_{0,\mathrm{e}}$ (m^2/Vs)	c_{trap}	T_0 (K)
NHT5:NDP2	-5.10					
α-NPD	-5.33	-2.23	6×10^{-9}	6×10^{-10}		
α-NPD	-5.43	-2.33	6×10^{-9}	6×10^{-10}		
Ir(MDQ)$_2$(acac)	-5.13	-2.93	6×10^{-9}	6×10^{-10}		
TCTA	-5.60	-2.20	2×10^{-8}	2×10^{-9}		
Ir(ppy)$_3$	-5.20	-2.70	2×10^{-8}	2×10^{-9}		
TCTA	-5.60	-2.20	2×10^{-8}	2×10^{-9}		
TPBi	-6.20	-2.60	2×10^{-8}	2×10^{-9}		
Spiro-DPVBi	-5.70	-2.80	6×10^{-9}	8×10^{-9}	0.001	2350
NET5	-6.00	-2.50	1.5×10^{-11}	1.5×10^{-10}	0.005	1400
NET5:NDN1		-2.50				

Table 1: Material parameters: charge dynamics.

Material	k_{r} (μs^{-1})	k_{nr} (μs^{-1})	R_0 (nm)	E_{T} (eV)
Ir(MDQ)$_2$(acac)	0.588	0.112	1.5	2.0
Ir(ppy)$_3$	0.816	0.249	1.5	2.4

Table 2: Material parameters: exciton dynamics.